Applied Materials Today 41 (2024) 102430

Contents lists available at ScienceDirect

Applied Materials Today

journal homepage: www.elsevier.com/locate/apmt

Spinodally reinforced W-Cr fusion armour

Alexander J Knowles [a,b,c,*], Tat Yiu Spencer Cheung [b], Kan Ma [a], Russel Dodds [b], Samuel A Humphry-Baker [b], Felipe F. Morgado [d], Shyam S Katnagallu [d], Eduardo Saiz [b], Baptiste Gault [d,b], Christopher D Hardie [c], David Dye [b]

[a] School of Metallurgy & Materials, University of Birmingham, Birmingham B15 2SE, UK
[b] Department of Materials, Imperial College, South Kensington, London SW7 2AZ, UK
[c] UK Atomic Energy Authority, Abingdon, Oxfordshire OX14 3DB, UK
[d] Max-Planck-Institut für Eisenforschung GmbH, Max-Planck-Straße 1, Düsseldorf D-40237, Germany

ARTICLE INFO

Keywords:
Fusion energy
Tungsten alloys
Microstructure design
Spinodal decomposition

ABSTRACT

Here, we introduce a discontinuous spinodal reinforcement strategy in the novel candidate plasma facing material (PFM) of tungsten-chromium alloys. Thermal ageing of a W-34wt%Cr alloy at 1250 °C causes nano-scale lamellae 200–600 nm to form heterogeneously from grain boundaries, which progressively grow into the matrix fully, then coarsen to 1–2 μm after 100 h. The dual-phase microstructure confers exceptional high temperature compressive strength, maintaining 900 MPa at 1000 °C - double that of polycrystalline tungsten. Further, the chromium alloying promotes a dense oxide scale that confers a 2 orders of magnitude improvement in resistance against oxidation at 1000 °C compared to W, which is an important consideration for PFMs under loss of vacuum accident conditions. The dual-phase W-Cr alloy concept's combination of high strength and oxidation resistance represents a new scalable alternative to tungsten, with wide scope for further alloying and process optimisation.

1. Introduction

Despite major recent achievements for various fusion power plant concepts [1–3], many challenges remain, in particular, how the structure and materials will survive and extract energy from the 150-million--celsius plasma, whilst surviving for >20-year design lifetimes. Tungsten (W) is the leading fusion plasma-facing material (PFM), particularly for the divertor [4]. W is selected for its high melting point; high ionisation energy – minimising loss & pollution of the plasma; low solubility for hydrogen - minimising tritium retention; and low activation following fusion neutron irradiation - avoiding production of long-lived radioactive waste. However, tungsten has challenges: mechanically, to ensure sufficient high-temperature strength and creep resistance, and critically with its high ductile to brittle transition (DBTT) temperature of 300–700 °C [5] – which becomes yet worse following irradiation [6]; further, W has poor oxidation resistance - in the event of a loss of coolant/vacuum accident (LOCA / LOVA) [7], with tungsten oxide subliming at temperatures >1000 °C [8], this is a particular concern alongside the high decay heat from short-lived tungsten isotopes present following operation, which would lead to hours-to-days at 900–1200 °C after shut-down [9].

Tungsten's performance was greatly improved through the 20th century, driven notably by the incandescent filament light bulb industry [5,10]. Beyond purity and interstitial reductions, submicron grain sizes obtained by drawing optimisation and inclusion control can bring about ductility at room temperature [11], however, the large strain reduction levels are only readily obtainable in thin sections, rather than larger parts, e.g. plates, needed for the fusion first wall & divertor. Other grain control approaches have achieved some success, notably W fibre + W matrix composites [12], or multilayer laminates [13], as well as oxide or carbide dispersion strengthening (ODS/CDS) [5,14–17], which improve irradiation damage resistance thanks to the high interface density. However, there are challenges in the scalability and cost of these approaches.

Alloying is another strategy to bring about improved properties. Rhenium additions are well known to offer potent improvements in ductility whilst maintaining high melting point and strength [8,18], however, Re is expensive ~$2000/kg, and the ductilising benefit is lost following irradiation at intermediate temperatures due to precipitate formation [18,19]. Other solid solution alloying elements have been investigated, as reviewed by Ren et al. [5], e.g. Ta, V, and Ti, but none confer an analogous benefit to Re. High Entropy Alloy (HEA), may offer

* Corresponding author at: School of Metallurgy & Materials, University of Birmingham, Birmingham B15 2SE, UK.
E-mail address: a.j.knowles@bham.ac.uk (A.J. Knowles).

https://doi.org/10.1016/j.apmt.2024.102430
Received 1 July 2024; Received in revised form 29 August 2024; Accepted 7 September 2024
Available online 12 September 2024

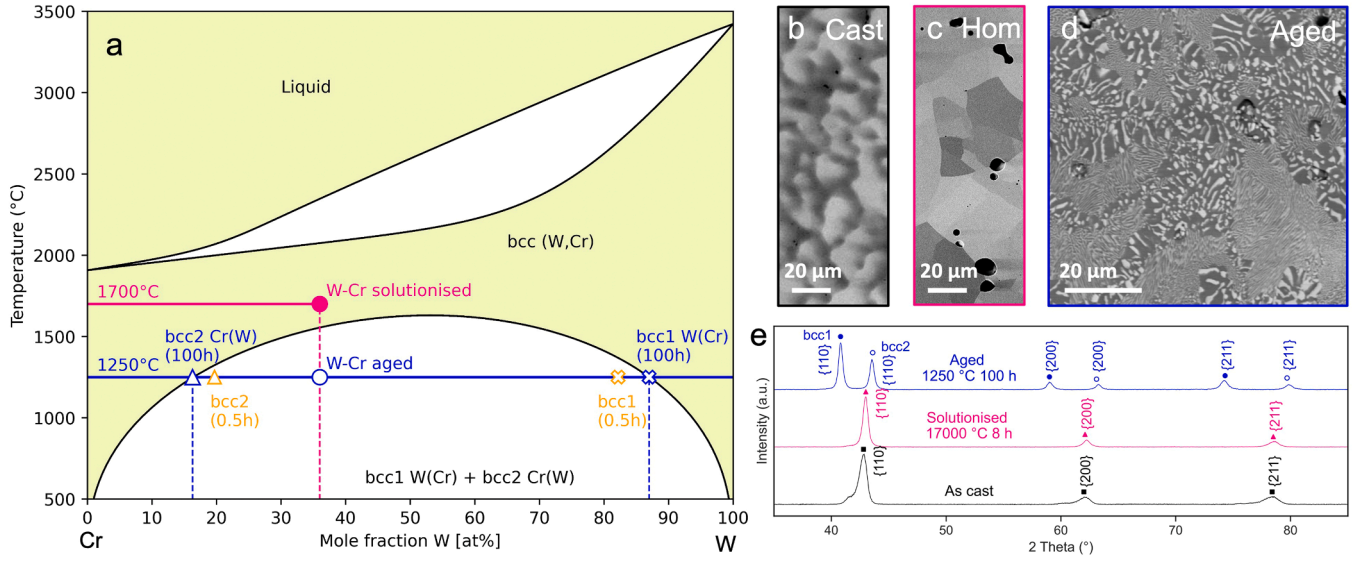

Fig. 1. W-Cr (a) Binary phase diagram calculated using Thermocalc TCHEA6 database, with the gas phase of Cr omitted. SEM BSE micrographs of the W-Cr alloy (b) as-cast condition, (c) solution heat treated (Hom) at 1700 °C for 8 h, and then (d) aged 1250 °C 100 h, with (e) corresponding XRD patterns with bcc reflections.

a new design basis addressing the DBTT in body-centred cubic (bcc) metals, with new ductility criteria being proposed by Mak, Yin & Curtin [20]. However, there are critically few experimental investigations of DBTT in refractory HEAs (RHEAs). HEAs may offer further benefits, notably on reduced irradiation hardening [21–23]. Combining grain size control with alloying, the works of Park & Schuh et al. [24,25] have proposed phase-separating nanostructured alloys including W-Cr. This approach of 'top down' refinement uses mechanical alloying to create a solid solution, with two-phase decomposition on ageing trapping a nano-scale structure. Single-phase W-Cr has also attracted interest from groups investing 'smart' tungsten alloys to address W's rapid oxidation under loss-of-coolant and air ingress accidents in a fusion reactor, as recently demonstrated in single-phase alloys [26,27].

However, challenges remain across the design strategies to simultaneously balance processability, strength, ductility, oxidation and irradiation resistance in W-based alloys. Here, we introduce a scalable approach in the W-Cr system designed to exploit spinodal decomposition on thermal ageing, following a single-phase solution heat treatment; to simultaneously enhance mechanical properties through 'bottom up' nano-scale reinforcement by phase-decomposition; alongside oxidation resistance against accident scenarios by formation of a protective chromia scale.

2. Methods

25 g ingots were prepared by vacuum arc melting of pure elements (> 99.9%) under Ar, by ACI Alloys Inc, to a target compositions of W-42.1 wt%Cr (28 at.%W-72 at.%Cr) designed to be within the spinodal miscibility gap between A2 W(Cr) and A2 Cr(W). The density was found to be 11.2 g cm^{-3}, determined using the Archimedes method. The ingots were sectioned and then solution heat treated at 1700 °C in a tungsten element Thermal Technology LLC high temperature Furnace. An alumina crucible was used, the chamber was evacuated and backfilled with Ar gas that was maintained at a pressure between 4 and 10 psi throughout the heat treatment. The heating rate was 10 °C/min and held at the temperature for the designated duration; an actuator then transferred the sample from the upper heating chamber to an unheated lower chamber, achieving a cooling rate estimated to be 100 °C/min. Sections for ageing were encapsulated within evacuated glass ampoules backfilled with argon prior to heat treatment at 1250 °C for various times followed by water quenching.

Microstructure characterisation was performed using scanning electron microscopy (SEM) on a Zeiss Sigma operated at 10 kV for imaging, and a JEOL 5800 operated at 20 kV for energy dispersive X-ray spectrometry (EDX). The bulk composition was evaluated using SEM-EDS by measuring the overall composition of 5 areas scans 200 × 200 μm^2 across the ingot, these were averaged, leading to a composition of 35.8 ± 3.5W-64.2 ± 3.5Cr at.% (± standard deviation). For impurity analysis, we used a 'LECO Corporation' (www.leco.com) combustion analyser. Interstitials were found to be 57 ppm C, 214 ppm N and 522 ppm O. X-ray diffraction (XRD) was performed using a BRUKER D2 PHASER to determine the phases present in the alloy and their lattice parameters ±0.0001 nm using Cu-K_α radiation on flat samples ~ 8 mm in diameter. The binary phase diagram was calculated using the TCTI3 database in the Thermocalc software to determine the compositions of phases at equilibrium conditions.

Transmission electron microscopy (TEM) and scanning TEM (STEM) were performed on a JEOL 2100F microscope operated at 200 kV. Electron transparent foils were prepared from 3 mm discs to 150 µm electropolished using a twin-jet electropolishing unit, using a solution of 10 % perchloric acid in methanol at a temperature of −30 °C. Due to the electropolishing preparation method some W phase was removed leaving dark elongated holes (Fig. 3c). In addition, multiple spots appear around each plane reflection that are attributed to 'double diffraction' [46]. Double diffraction occurs in nano-structures that have a similar length scale to the TEM foil thickness [45], while some additional reflections result from the lattice parameter difference between W(Cr) and Cr(W) bcc phases, and this may also drive a small misorientation between the lattices. Atom probe tomography (APT) samples ~100 × 100 × 1000 nm were prepared using a Ga focus ion beam (FIB) extraction method [30]. The experiments were conducted using pulsing laser mode in the Cameca LEAP 5000 XS instrument. The temperature was around 40 K, laser energy of 110 pJ, and pulsed rate of 200 kHz.

Hardness testing used a 1 kg load held for 10 s, averaging five indent measurements, with standard deviations as error bars, as shown in Fig. 2e. High temperature properties were investigated by compression testing using a MRF Inc. vacuum furnace maintained with a pressure below 5.4 × 10^{-8} MPa, heated at a rate of 20 °C/min and equilibrated at the set-point for 10 min prior to compression, with the temperature monitored by a W-WRe thermocouple. The load was applied using graphite push rods attached to an Instron universal tester with a 25 kN 2527 Series load cell. Samples were 2 × 2 × 2 mm cuboids prepared using electro discharge machining followed by light grinding to remove surface damage. Samples were sandwiched between 3 mm SiC spacers to

Table 1
Composition of the two bcc phases in the W-Cr alloy aged at 1250 °C for 100 h and 30 min. The data from phase diagram were generated using TCTI3 database in the Thermocalc software.

Ageing time	Equilibrium		100 h		30 min	
Methods	Phase diagram		XRD (Vegard's law)		APT	
Elements (at.%)	W	Cr	W	Cr	W	Cr
bcc1	83.7	16.3	86.1	13.9	82.2	17.8
bcc2	13.0	87.0	18.6	81.4	19.5	80.3

protect the push rods. Test were carried out at fixed displacement rate of 0.2 mm/min, corresponding to a nominal strain rate of $\sim 10^{-3}$ s^{-1}. The compressive proof stress was calculated using the 0.2% offset method. Compliance of the push rods was accounted for by using a linear fit to the elastic portion of the load-displacement curve.

Oxidation performance was evaluated on 2 × 2 × 2 mm cuboidal samples tested in a STA 449 F5 Jupiter Thermogravimetric Analyser (TGA). The sample was held within an alumina crucible and first heated to 1000 °C in Ar and held isothermally. After a 10 min temperature stabilisation period, air was flowed over the sample at rate of 100 ml/min for a 2 h duration, after which the sample was again purged with Ar before cooling.

3. Results and discussion

3.1. Alloy design & microstructure

A W-Cr alloy with composition 66W-34Cr (weight percent, wt.%), i.e. 36W-64Cr (atomic percent, at.%), was selected to exploit the wide miscibility gap in the W-Cr binary system between a body-centred cubic (bcc) (W,Cr) and bcc (Cr,W) below 1630 °C, as identified on the W-Cr phase diagram in Fig. 1a. The alloy was produced by arc melting with interstitial impurities C, N and O found to be 57, 214 and 522 ppm respectively. It results in an as-cast structure of W-rich dendrites, revealed by atomic number (Z) contrast backscattered-electron (BSE) SEM imaging in Fig. 1b. Solution heat treatment for 8 h at 1700 °C, was successful at interdiffusing the W and Cr to achieve the target single-phase bcc solid solution, WCr(Hom), with some limited residual porosity ~5 area% as shown in Fig. 1c. A single-phase bcc solid solution is an important characteristic for industrial scale-up, to enable bulk thermomechanical processing of large sections, reproducibility, and better control of the resulting physical properties. Subsequent ageing at 1250 °C for 100 h resulted in the intended phase separation, producing two bcc phases, one W-rich (bright owing to high atomic number contrast), the other Cr-rich (darker), visible in electron micrographs, Fig. 1d. This was further confirmed by XRD (Fig. 1e), where reflections for two bcc phases, bcc1 and bcc2, were observed with lattice parameters $a_{bcc1} = 0.3131$ and $a_{bcc2} = 0.2942$ nm ±0.001 nm. Lattice misfit δ can be deduced as $\delta=(a_{precipitate}-a_{matrix})/ a_{matrix}$ [28], with the W-rich phase as the precipitate phase and the Cr-rich phase as the matrix phase, leading to a lattice misfit δ = 6 %. Using Vegard's law, the composition of the two bcc phases were 86.1W-13.9Cr and 18.6W-81.4Cr (at.%) respectively, which are close to the Thermocalc-derived compositions marked in Fig. 1a. The experimental results are summarised in Table 1, and are also close to the miscibility boundary predicted by the model of Turchi et al. [29] of 84.5W-15.5Cr and 14.7W-85.3Cr(at.%). Thus, the two phases were annotated as bcc1 W(Cr) and bcc2 Cr(W). To study the

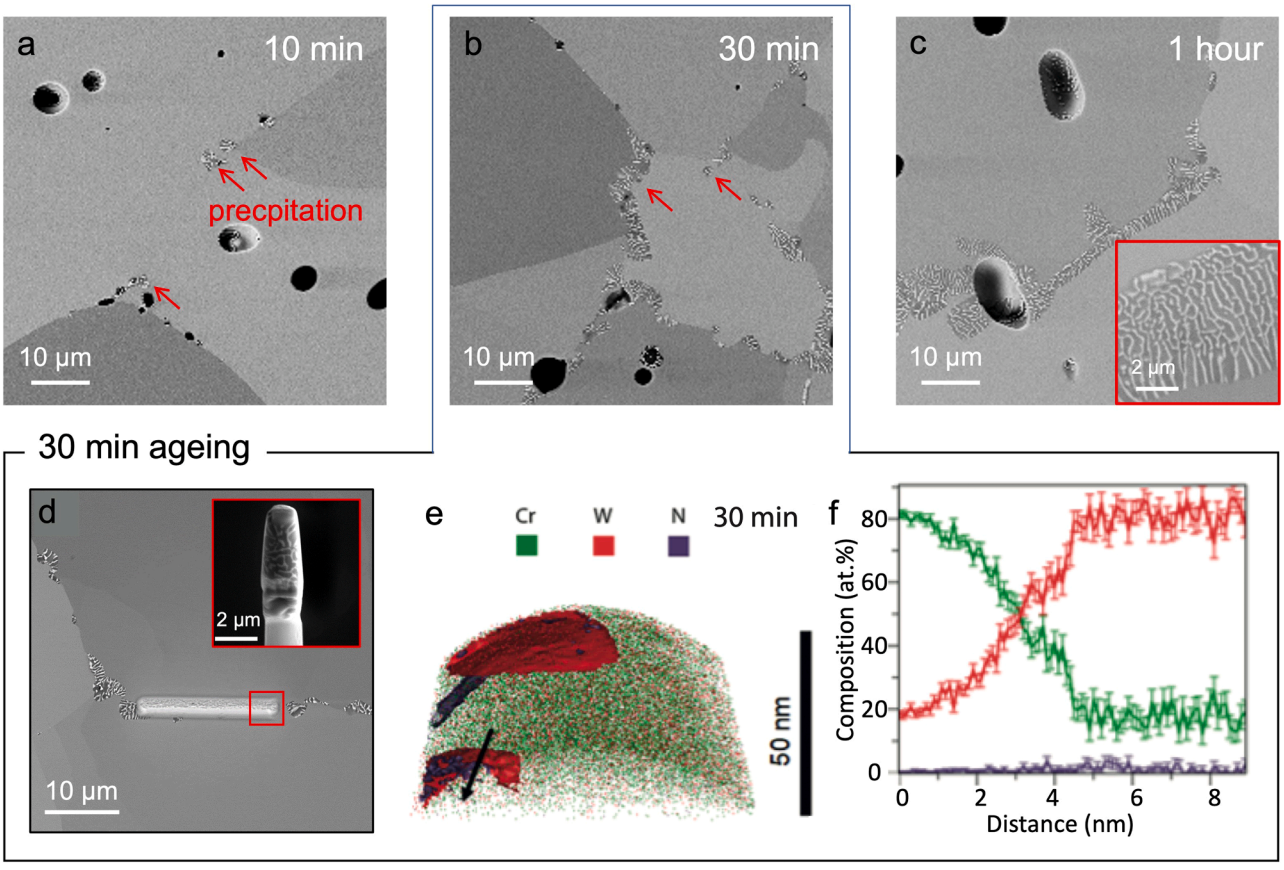

Fig. 2. Microstructure characterisation of the W-Cr alloy aged at 1250 °C for (a) 10 min, (b) 30 min and (c) 1 h with high-magnification inset showing the sub-micrometer lamellar structure. (d) SEM BSE image of an alloy aged for 30 min showing the lift-out area for Atom Probe Tomography (APT) experiment with the needle sample lifted from the red rectangle area at grain boundaries with lamellae decomposition. Inset SEM image showing a half-milled APT needle with lamellae. (e) Element maps by APT with (f) line profiles along the corresponding black arrow (out of scale) through a W-rich region.

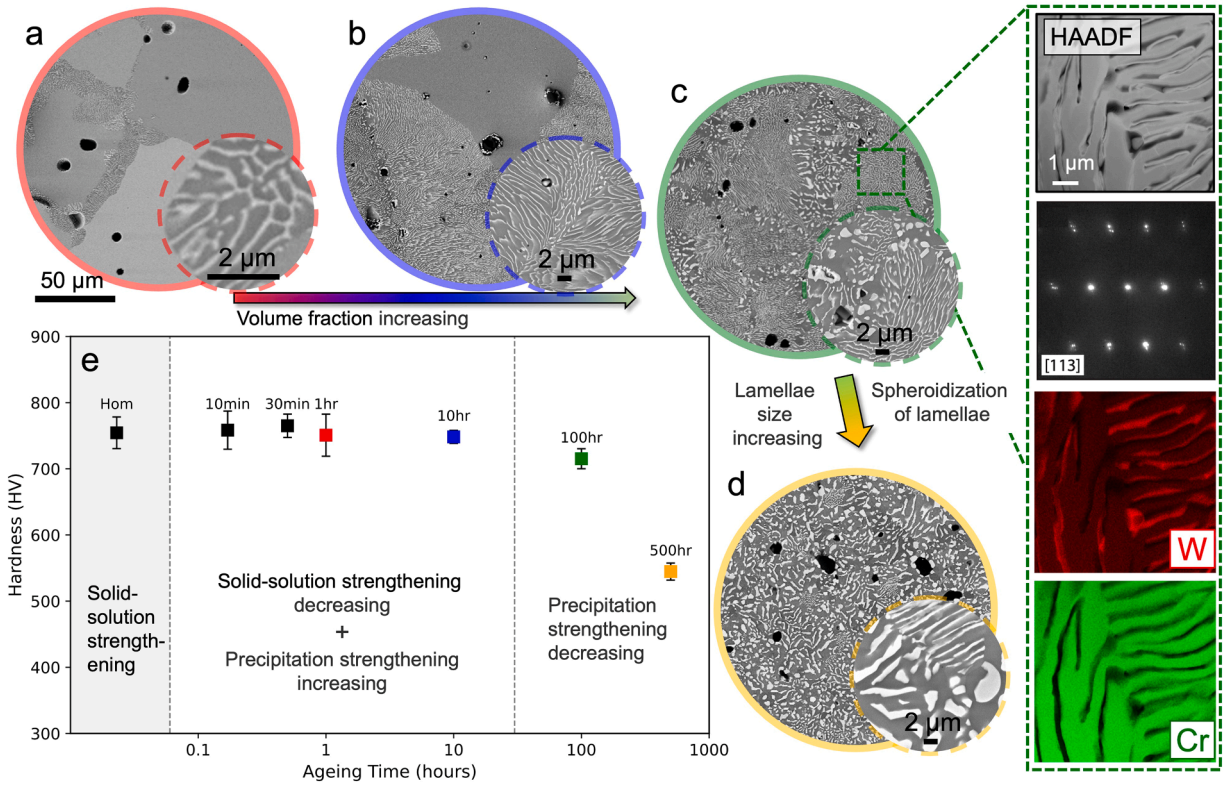

Fig. 3. SEM BSE micrographs of the W-Cr alloys following ageing at 1250 °C for (a) 1 h, (b) 10 h, (c) 100 h and (d) 500 h, and (e) hardness change on ageing (HV 1 kg, with S.D. error bars). Inset image in (c) shows the STEM/HAADF observation with corresponding STEM/EDS element maps and selected diffraction patterns along ⟨113⟩ zone axis.

bcc -> bcc1+bcc2 decomposition reaction in more detail, interrupted early-stage and extended ageing experiments at 1250 °C were employed, from 10 min to 500 h.

3.2. *Microstructure formation and evolution*

Early phase decomposition from 10 min to 1 h ageing developed a fine lamellae microstructure of 200–600 nm lamellar spacing, initiated from grain boundaries, Fig. 2 (a–c). Atom probe tomography (APT) was used to gain insights into the early stages of the nucleation process by analysing 30 min aged samples. APT specimens from the grain boundary region were prepared following the protocols in [30] (Fig. 2d). The target phases bcc1 W(Cr) and bcc2 Cr(W) regions were observed in the 30 min aged APT sample as shown in Fig. 2b, with compositions of 82.2W-17.8Cr and 19.5W-80.3Cr at.% respectively. Contrast to the near-equilibrium status in the alloy aged for 100 h by XRD, the APT data of the bcc1 W(Cr) and bcc2 Cr(W) phases aged for 30 min indicated a non-equilibrium composition of the early nuclei at the grain boundaries (Fig. 1a). In addition, the APT revealed nitrogen-rich nano-domains with ~5 at.% nitrogen (N) in both samples aged for 30 min (Fig. 2e, purple features). LECO composition measurement found a low bulk nitrogen concentration of 214 ppm. The manufacturing process, conditions and raw elements were selected to minimise interstitial contents, as they are known to have a strong influence on the properties of refractory metals [31–33]. It is suggested that nitrogen preferentially segregates to grain boundaries, amplified by a change in solubility with temperature and/or between decomposing phases, leading to formation of the N-rich domains, which may partially enhance the heterogeneous grain boundary nucleation [34,35]. In addition to the influence on spinodal nucleation, the N-rich phases may act as secondary barriers to dislocations and harden grain and phase boundaries [36].

The long-term evolution of the microstructure with ageing was tracked from 1 h to 500 h, Fig. 3 (a–d). Performing prolonged heat treatment durations is important to evaluate the microstructure evolution under long-term conditions, aligning with the high-temperature operation in fusion applications. After ageing for 10 h the fine lamellae continued to grow, gradually consuming the prior single-phase domains (Fig. 3b). This is suggestive of a discontinuous spinodal decomposition., initiated from grain boundaries, is similar to the report of Porter [37], rather than a bulk homogenous spinodal decomposition. Discontinuous spinodal, or cellular precipitation, whereby nucleation occurs at grain boundaries (rather than homogeneously in the bulk in a classical spinodal), and then grows out into the bulk, resulting in a pearlite-like microstructure [38–41]. It was suggested that, due to grain boundary-enhanced atomic mobility, discontinuous spinodal decomposition occurs when the grain boundary acts as a moving transformation front, creating a lamellar microstructure. After 100 h, the prior single-phase grains were fully consumed by the decomposition, with much of the earlier finer lamellae of 200–600 nm having coarsened to a 1–2 μm lamellar spacing, with the coarsened two-phase structure becoming the majority microstructure after 500 h, Fig. 3 (c and d). The anticipated Cr-rich and W-rich separated lamellae in the 100 h aged sample are evidenced by STEM/EDS mapping in the inset image of Fig. 3c. Selected area diffraction found close alignment of the two crystal lattices following a $(001)_{bcc\ (W,Cr)}//(001)_{bcc\ (Cr,W)}$ orientation relationship, despite the misfit of $\delta = 6$ % recorded by XRD (Fig. 1e), which resulted in separated diffraction spots.

3.3. *Mechanical properties*

The high-temperature capability of the alloys was assessed using mechanical and environmental testing. Despite substantial changes in the microstructure with ageing times up to 10 h, the hardness of the alloy remained ~750 HV, Fig. 3e. Whilst precipitation age hardening is expected, minimal change in hardness was observed up to 10 h, which may be due to an accompanying loss in solid solution strengthening as

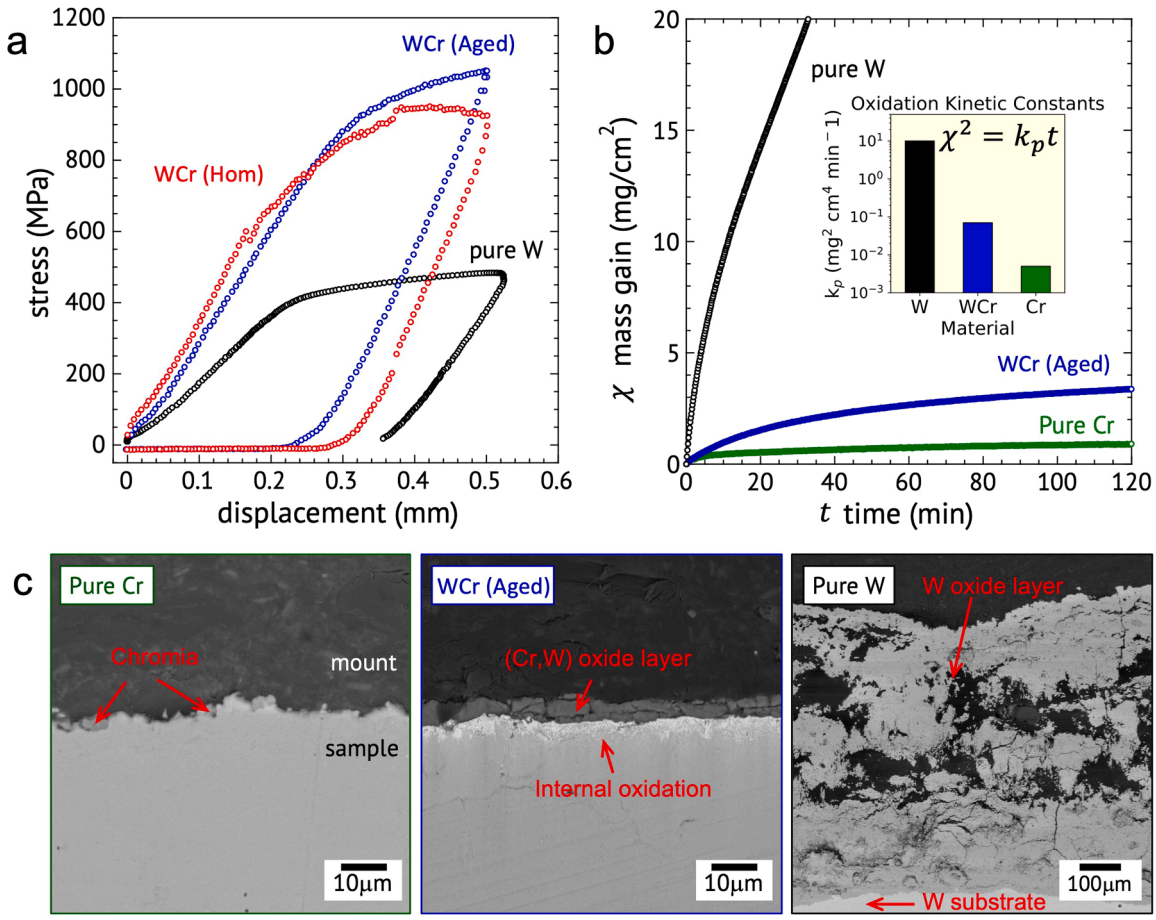

Fig. 4. High temperature behaviour of W-Cr alloy. (a) Hot compression strength at 1000 °C of the W-Cr solution heat treated alloy WCr(Hom) and aged alloy WCr (aged), with polycrystalline W benchmark, (b) Oxidation performance by thermogravimetric analysis (TGA) in air at 1000 °C, with W and Cr benchmarks, and (c) respective SEM oxide cross sections after TGA testing.

the decomposed domains form. In contrast, from 10 to 500 h a pronounced loss in hardness occurs, attributed to the coarsening of the two-phase microstructure and so reduced Orowan strengthening.

The mechanical properties at the macroscopic scale at high temperatures were investigated using hot compression testing performed under vacuum at 1000 °C. Fig. 4a presents displacement-stress curve of the single-phase solution heat treated WCr(Hom) alloy, which exhibits a remarkable 0.2 % proof compressive strength of >600 MPa. This greatly exceeds the polycrystalline W benchmark (<400 MPa), and the archetypical nickel-based superalloys (<200 MPa at 1000 °C) [42,43]. Furthermore, the dual-bcc-phase microstructure WCr(Aged) arising from the ageing at 1250 °C for 100 h further increases the yield strength to approximately 900 MPa at 1000 °C, double that of W. This ~300 MPa increase from the solution heat treated alloy confirms that spinodal reinforcement is an effective high temperature strengthening strategy, though the room temperature micro-hardness values remained similar. For the room temperature hardness there is initial little change with ageing up to 10 h, attributed to a trade-off between solid solution solute hardening being lost as the second-phase hardening is gained, as well as high hardness anticipated due to being below DBTT that may mask some of the microstructure hardening changes. From 10 to 100 to 500 h the sequential decrease in hardness is attributed to reducing second-phase strengthening due to coarsening, and reaching a minimum solid solution strengthening. While in the high-temperature compression testing, in the aged versus solutionised condition, the aged alloy has an additional strengthening mechanism due to the second phase reinforcement acting as a barrier to dislocations.

3.4. Oxidation resistance

The environmental resistance of the alloy toward a LOVA/LOCA scenario was evaluated by isothermal oxidation at 1000 °C as shown in the thermogravimetric analysis (TGA) in Fig. 4b. The aged WCr(spin) alloy exhibited a parabolic oxidation profile owing to the formation of a self-protecting chromia scale. This resulted in a 2 order of magnitude improvement in oxidation performance compared to pure tungsten and came close (within a factor of 10) to the pure Cr control sample. The parabolic rate constants of the W, WCr(spin) and Cr were about 10, 0.07 and 0.005 mg^2/cm^4/min respectively. The cross-sectional micrographs in Fig. 4c support the TGA data, showing scale thickness of ~700, 5 and 1 µm respectively. Meanwhile the oxide scale of the WCr spinodal alloy is dense and homogenous, indicating it will continue to provide protection for longer durations, unlike the scale of pure W, which is porous. It is likely that the region labelled “internal oxidation” is depleted in Cr due to its light contrast; further high-magnification images of this region are given in Supplementary Fig. 1. In addition chromia in the scale, some Cr_2WO_6 and WO_3 could have formed, as was observed for a W-Cr alloy in [44] at the same oxidation temperature. The TGA data for the solutionised W-Cr sample is shown in Supplementary Fig. 2. It shows clear evidence of the volatility of some W oxides as the sample lost mass during the test presumably as the volatilisation occurred at a greater rate than the mass gain due to tungsten and chromium oxide formation. Overall, Fig. 4 reveals that this alloy design gives a remarkable high-temperature property balance, with the yield strength being double that of W, paired with the oxidation rate constant being two orders of magnitude lower than W.

4. Conclusion

In conclusion, we exploited the miscibility gap in a W-Cr alloy for a controlled phase decomposition at 1250 °C to generate a tuneable micron/nano-scale microstructure of bcc (W,Cr) + bcc (Cr,W), following a single-phase solution heat treatment at 1700 °C. The formation occurred as a discontinuous spinodal decomposition akin to discontinuous precipitation, forming fine lamellae initiated from grain boundaries. Atom probe tomography highlighted the influence of 5 nm N-rich domains at grain boundaries which influence the nucleation & strengthening. The two-phase microstructure provided the alloy with an exceptional high temperature compressive strength of ~900 MPa at 1000 °C, greatly exceeding the benchmark performance of W. Oxidation resistance was found to be two orders of magnitude slower compared to pure W, coming close to elemental Cr, owing to the formation of a dense and protective chromia-rich scale on the W-Cr alloy. Spinodal W-Cr alloys can be further alloyed to improve their properties; for oxidation properties with Ti or Y [7,26], or reinforcement via oxide/carbide particle dispersion strengthening (ODS/CDS) [5,14] or precipitate strengthening [45]. Further work will help balance oxidation resistance & strength alongside the other properties of the alloys, such as toughness and irradiation resistance.

CRediT authorship contribution statement

Alexander J Knowles: Writing – original draft, Supervision, Methodology, Investigation, Funding acquisition, Conceptualization. **Tat Yiu Spencer Cheung:** Writing – review & editing, Validation, Investigation. **Kan Ma:** Writing – review & editing, Visualization, Validation. **Russel Dodds:** Writing – review & editing, Validation, Investigation. **Samuel A Humphry-Baker:** Writing – review & editing, Visualization, Validation, Investigation. **Felipe F. Morgado:** Investigation, Formal analysis. **Shyam S Katnagallu:** Investigation, Formal analysis. **Eduardo Saiz:** Writing – review & editing, Investigation. **Baptiste Gault:** Writing – review & editing, Investigation, Formal analysis. **Christopher D Hardie:** Writing – review & editing, Supervision, Resources, Funding acquisition, Conceptualization. **David Dye:** Writing – review & editing, Supervision, Funding acquisition, Conceptualization.

Declaration of competing interest

The authors declare that they have no known competing financial interests or personal relationships that could have appeared to influence the work reported in this paper.

Data availability

Data will be made available on request.

Acknowledgements

This work was supported by A Knowles' EUROfusion Researcher Grant Fellowship (AWP17-ERG-CCFE/Knowles), UKRI Future Leaders Fellowship (MR/T019174/1), and Royal Academy of Engineering Research Fellowship (RF\201819\18\158). S.H-B acknowledges support from a UK Engineering and Physical Sciences Research Council (EPSRC) Open Fellowship (Grant number EP/ W008025/1). F.F.M. acknowledges financial support from the International Max Planck Research and School for Interface Controlled Materials for Energy Conversion (IMPRSSurMat). The authors are grateful to Uwe Tezins, Christian Broß, and Andreas Sturm for their support to the FIB and APT facilities at MPIE.

Supplementary materials

Supplementary material associated with this article can be found, in the online version, at doi:10.1016/j.apmt.2024.102430.

References

[1] E. Gibney, Fuel for world's largest fusion reactor ITER is set for test run, Nature 591 (2021) 15–16.
[2] E.I. Moses, The National Ignition Facility (NIF): a path to fusion energy, Energy Convers. Manag. 49 (2008) 1795–1802.
[3] H. Wilson, I. Chapman, T. Denton, W. Morris, B. Patel, G. Voss, C. Waldon, STEP Team, STEP—on the pathway to fusion commercialization. Commercialising Fusion Energy: How Small Businesses are Transforming Big Science, IOP Publishing Bristol, UK, 2020, 8–1.
[4] D. Stork, P. Agostini, J.-L. Boutard, D. Buckthorpe, E. Diegele, S.L. Dudarev, C. English, G. Federici, M.R. Gilbert, S. Gonzalez, Materials R&D for a timely DEMO: key findings and recommendations of the EU roadmap materials assessment group, Fusion Eng. Design 89 (2014) 1586–1594.
[5] C. Ren, Z.Z. Fang, M. Koopman, B. Butler, J. Paramore, S. Middlemas, Methods for improving ductility of tungsten-a review, Int. J. Refract. Met. Hard Mater. 75 (2018) 170–183.
[6] R. Abernethy, J.-L. Gibson, A. Giannattasio, J. Murphy, O. Wouters, S. Bradnam, L. Packer, M. Gilbert, M. Klimenkov, M. Rieth, Effects of neutron irradiation on the brittle to ductile transition in single crystal tungsten, J. Nucl. Mater. 527 (2019) 151799.
[7] D. Liu, L. Zheng, L. Luo, X. Zan, J.-P. Song, Q. Xu, X. Zhu, Y. Wu, An overview of oxidation-resistant tungsten alloys for nuclear fusion, J. Alloys Compd. 765 (2018) 299–312.
[8] J. Berkowitz, W.A. Chupka, M.G. Inghram, Polymeric gaseous species in the sublimation of tungsten trioxide, J. Chem. Phys. 27 (1957) 85–86.
[9] D. Maisonnier, I. Cook, S. Pierre, B. Lorenzo, B. Edgar, B. Karin, F. Robin, G. Luciano, H. Stephan, N. Claudio, The European power plant conceptual study, Fusion Eng. Design 75 (2005) 1173–1179.
[10] P. Schade, 100 years of doped tungsten wire, Int. J. Refract. Met. Hard Mater. 28 (2010) 648–660.
[11] D.B. Snow, The recrystallization of commercially pure and doped tungsten wire drawn to high strain, Metallur. Trans. A 10 (1979) 815–821.
[12] J. Riesch, Y. Han, J. Almanstötter, J. Coenen, T. Höschen, B. Jasper, P. Zhao, C. Linsmeier, R. Neu, Development of tungsten fibre-reinforced tungsten composites towards their use in DEMO—Potassium doped tungsten wire, Phys. Scr. 2016 (2016) 014006.
[13] J. Reiser, M. Rieth, B. Dafferner, A. Hoffmann, Tungsten foil laminate for structural divertor applications–basics and outlook, J. Nucl. Mater. 423 (2012) 1–8.
[14] T. Zhang, Z. Xie, J. Yang, T. Hao, C. Liu, The thermal stability of dispersion-strengthened tungsten as plasma-facing materials: a short review, Tungsten 1 (2019) 187–197.
[15] H. Kurishita, S. Kobayashi, K. Nakai, T. Ogawa, A. Hasegawa, K. Abe, H. Arakawa, S. Matsuo, T. Takida, K. Takebe, Development of ultra-fine grained W–(0.25–0.8) wt% TiC and its superior resistance to neutron and 3 MeV He-ion irradiations, J. Nucl. Mater. 377 (2008) 34–40.
[16] M. Battabyal, P. Spätig, B.S. Murty, N. Baluc, Investigation of microstructure and microhardness of pure W and W-2Y2O3 materials before and after ion-irradiation, Int. J. Refract. Met. Hard Mater. 46 (2014) 168–172, https://doi.org/10.1016/j.ijrmhm.2014.06.004.
[17] E. Lang, N. Madden, C. Smith, J. Krogstad, J.P. Allain, Deciphering the role of second phase precipitates on early-stage surface morphology development of dispersion-strengthened W alloys under low energy He irradiation, Nucl. Mater. Energy 19 (2019) 47–54, https://doi.org/10.1016/j.nme.2019.01.016.
[18] D. Armstrong, X. Yi, E. Marquis, S. Roberts, Hardening of self ion implanted tungsten and tungsten 5-wt% rhenium, J. Nucl. Mater. 432 (2013) 428–436.
[19] M.J. Lloyd, R.G. Abernethy, D.E.J. Armstrong, P.A.J. Bagot, M.P. Moody, E. Martinez, D. Nguyen-Manh, Radiation-induced segregation in W-Re: from kinetic Monte Carlo simulations to atom probe tomography experiments, Eur. Phys. J. B 92 (2019) 241, https://doi.org/10.1140/epjb/e2019-100244-y.
[20] E. Mak, B. Yin, W. Curtin, A ductility criterion for bcc high entropy alloys, J. Mech. Phys. Solids 152 (2021) 104389.
[21] O. El-Atwani, N. Li, M. Li, A. Devaraj, J. Baldwin, M.M. Schneider, D. Sobieraj, J. S. Wróbel, D. Nguyen-Manh, S.A. Maloy, Outstanding radiation resistance of tungsten-based high-entropy alloys, Sci. Adv. 5 (2019) eaav2002.
[22] S. Zhao, Defect properties in a VTaCrW equiatomic high entropy alloy (HEA) with the body centered cubic (bcc) structure, J. Mater. Sci. Technol. 44 (2020) 133–139.
[23] T.-X. Li, J.-W. Miao, E.-Y. Guo, H. Huang, J. Wang, Y.-P. Lu, T.-M. Wang, Z.-Q. Cao, T.-J. Li, Tungsten-containing high-entropy alloys: a focused review of manufacturing routes, phase selection, mechanical properties, and irradiation resistance properties, Tungsten 3 (2021) 181–196.
[24] M. Park, K.C. Alexander, C.A. Schuh, Diffusion of tungsten in chromium: experiments and atomistic modeling, J. Alloys Compd. 611 (2014) 433–439.
[25] M. Park, C.A. Schuh, Accelerated sintering in phase-separating nanostructured alloys, Nat. Commun. 6 (2015) 6858.
[26] A. Litnovsky, T. Wegener, F. Klein, C. Linsmeier, M. Rasinski, A. Kreter, B. Unterberg, M. Vogel, S. Kraus, U. Breuer, Smart alloys for a future fusion power plant: first studies under stationary plasma load and in accidental conditions, Nucl. Mater. Energy 12 (2017) 1363–1367.

[27] A. Calvo, C. García-Rosales, N. Ordás, I. Iturriza, K. Schlueter, F. Koch, G. Pintsuk, E. Tejado, J.Y. Pastor, Self-passivating W-Cr-Y alloys: characterization and testing, Fusion Eng. Design 124 (2017) 1118–1121.
[28] A.J. Knowles, T.-S. Jun, A. Bhowmik, N.G. Jones, T.B. Britton, F. Giuliani, H. J. Stone, D. Dye, A new beta titanium alloy system reinforced with superlattice intermetallic precipitates, Scr. Mater. 140 (2017) 71–75, https://doi.org/10.1016/j.scriptamat.2017.06.038.
[29] P.E. Turchi, L. Kaufman, Z.-K. Liu, Modeling of Ni–Cr–Mo based alloys: part I—Phase stability, Calphad 30 (2006) 70–87.
[30] K. Thompson, D. Lawrence, D. Larson, J. Olson, T. Kelly, B. Gorman, In situ site-specific specimen preparation for atom probe tomography, Ultramicroscopy 107 (2007) 131–139.
[31] C. Bonnekoh, A. Hoffmann, J. Reiser, The brittle-to-ductile transition in cold rolled tungsten: on the decrease of the brittle-to-ductile transition by 600K to −65°C, Int. J. Refract. Met. Hard Mater. 71 (2018) 181–189, https://doi.org/10.1016/j.ijrmhm.2017.11.017.
[32] J.R. Stephens, Effects of Interstitial Impurities on the Low-Temperature Tensile Properties of Tungsten, National Aeronautics and Space Administration, 1964.
[33] P. Burdon, G. Davis, Embrittlement of Tungsten and of Molybdenum, Nature 185 (1960) 455.
[34] T. Sreenivas, K. Srinivas, R. Natarajan, N. Padmanabhan, An integrated process for the recovery of tungsten and tin from a combined wolframite–scheelite–cassiterite concentrate, Min. Process. Extract. Metallur. Rev. 25 (2004) 193–203.
[35] P. Zięba, Recent developments on discontinuous precipitation, Arch. Metall. Mater. 62 (2017) 955–968.
[36] A. Kumar, B.L. Eyre, Grain boundary segregation and intergranular fracture in molybdenum, Proc. R. Soc. Lond. A. Math. Phys. Sci. 370 (1980) 431–458.
[37] D. Porter, The decomposition of tungsten-chromium solid solution, Acta Metallur. 15 (1967) 721–726.
[38] H. Ramanarayan, T.A. Abinandanan, Phase field study of grain boundary effects on spinodal decomposition, Acta Mater. 51 (2003) 4761–4772, https://doi.org/10.1016/S1359-6454(03)00301-X.
[39] H. Ramanarayan, T. Abinandanan, Grain boundary effects on spinodal decomposition: II. Discontinuous microstructures, Acta Mater. 52 (2004) 921–930.
[40] S. Gorsse, P. Bellanger, Y. Brechet, E. Sellier, A. Umarji, U. Ail, R. Decourt, Nanostructuration via solid state transformation as a strategy for improving the thermoelectric efficiency of PbTe alloys, Acta Mater. 59 (2011) 7425–7437.
[41] A. Kwiatkowski da Silva, R.D. Kamachali, D. Ponge, B. Gault, J. Neugebauer, D. Raabe, Thermodynamics of grain boundary segregation, interfacial spinodal and their relevance for nucleation during solid-solid phase transitions, Acta Mater. 168 (2019) 109–120, https://doi.org/10.1016/j.actamat.2019.02.005.
[42] A.J. Knowles, L. Reynolds, V.A. Vorontsov, D. Dye, A nickel based superalloy reinforced by both Ni3Al and Ni3V ordered-fcc precipitates, Scr. Mater. 162 (2019) 472–476.
[43] "Inconel® Alloy 718 Datasheet," Tech. Rep. SMC-045, Special Metals, 2007.
[44] S. Telu, A. Patra, M. Sankaranarayana, R. Mitra, S. Pabi, Microstructure and cyclic oxidation behavior of W–Cr alloys prepared by sintering of mechanically alloyed nanocrystalline powders, Int. J. Refract. Met. Hard Mater. 36 (2013) 191–203.
[45] A.J. Knowles, D. Dye, R.J. Dodds, A. Watson, C.D. Hardie, S.A. Humphry-Baker, Tungsten-based bcc-superalloys, Appl. Mater. Today 23 (2021) 101014, https://doi.org/10.1016/j.apmt.2021.101014.
[46] C.B. Carter, D.B. Williams, Transmission Electron Microscopy: A Textbook for Materials Science, Springer Science & Business Media, 1996.